Preprocessing, Feature Extraction and Lithologic Mapping Using EO-1 Hyperion Data

ZHANG Xian-feng[1], PAZNER Micha[2]

[1] (*Institute of Remote Sensing and GIS, Peking University, Beijing* 100871) [2] (*University of Wes tern Ontario, London, Canada N6A 5C2*)

Abstract EO-1 Hyperion sensor is the first spaceborne hyperspectral instrument to acquire both VNIR and SWIR spectra. A Hyperion image which covers the middle part of the southeastern Chocolate Mountains district and the Rainbow mine area was used to evaluate the utility of Hyperion imagery in identifying gold-related rock units in this area. A group of pre-Tertiary gneiss appears to be the favorable host of gold deposits in the district. Satellite mapping of gold-associated lithologic units is helpful for the search for gold and understanding the regional geology. Pre-processing aspects of Hyperion data before it can be used for information extraction were first addressed in the study. The data dimension was reduced for data redundancy removal and feature extraction. A supervised classifier was finally used to extract the lithologic units that are significant for gold exploration in the study area. The result shows that MLC classifier is efficient for the extraction of lithologic units from the Hyperion data in the study area, and the resultant rock units have excellent correlation with those on the geologic reference map. The MLC classifier creates a "hard" classification with an overall accuracy of 86% and a Kappa coefficient 0.81. This case study indicates that Hyperion data can achieve accurate mapping of gold-associated rock units in the southeastern Chocolate Mountains.

Keywords EO-1 Hyperion, lithologic mapping, vertical stripe noise, feature extraction

中图法分类号: TP751 **文献标识码**: A **文章编号**: 1006-8961(2007)06-0981-10

EO-1 Hyperion 数据的预处理、特征提取和岩性填图研究

张显峰[1] PAZNER Micha[2]

[1] (北京大学遥感与 GIS 研究所, 北京 100871) [2] (加拿大西安大略大学, 伦敦市, 加拿大, N6A 5C2)

摘 要 EO-1 Hyperion 传感器是第一个可以获取可见光与近红外以及短波红外波长范围光谱信息的星载高光谱传感器。本文以美国最早的金矿采矿区之一,加利福尼亚州东南巧克力山的 Rainbow 金矿区作为研究案例,探讨了 Hyperion 数据的预处理方法,专题信息提取与填图,评估了 Hyperion 高光谱数据在识别与金矿有关的岩性类型的应用价值。结果表明,本文所提出的 Hyperion 数据预处理方法是有效的,MNF 方法能有效用于 Hyperion 数据维数的降低和数据冗余的去除以及分类特征的提取。最大似然分类器能够有效地从 Hyperion 高光谱数据中提取与金矿相关的重要岩体信息,所得到的岩性单元与地质图上对应的岩性分布具有很好的一致性。岩体分类的总精度为 86%。该研究表明,Hyperion 高光谱数据能够很好识别有细微光谱差别的岩性,因而在地质学研究与找矿领域有着良好的应用前景。

关键词 EO-1 Hyperion 岩性填图 垂直条带噪声 特征提取

1 Introduction

For nearly two decades, hyperspectral sensors such as the Airborne Visible/Infrared Imaging Spectrometer (AVIRIS) have provided a wealth of information on terrestrial materials[1]. Examples of successful applications of hyperspectral imagery to

收稿日期:2005-11-18;**改回日期**:2006-03-28

第一作者简介:张显峰(1967~),男,博士,副教授,副主任。2005 年于加拿大西安大略大学获地理信息科学博士学位。目前从事遥感数据智能处理方法、高光谱遥感数据在岩性与矿物填图、生态参数估计与反演等研究工作,以及 RS、GIS 和 GPS 技术的集成与应用研究。已在国内外学术刊物发表遥感、GIS 和 GPS 技术有关的学术论文 40 余篇。E-mail: xfzhang@pku.edu.cn

difficult tasks include small target detection, material identification, discrimination among very similar classes, and estimation of biochemical or geophysical parameters[2]. However, high cost and unavailability of airborne hyperspectral data partly constrains the utility of hyperspectral data. The Hyperion sensor on board the NASA Earth Observing 1 (EO-1) satellite[3,4] is the first spaceborne hyperspectral instrument to acquire both visible near-infrared (VNIR) and shortwave infrared (SWIR) spectra. The EO-1 satellite co-orbits with the Landsat-7 satellite and Terra satellite. Hyperion is a pushbroom sensor with two spectrometers and a single telescope. Hyperion acquires 256-pixel images with a normal pixel size of 30m on the ground over a 7.65-km swath[5]. The first Hyperion spectrometer has 70 channels in the VNIR wavelength range, and the second one has 172 channels in the SWIR wavelength range. The spectral resolution is 10nm, which is identical to the AVIRIS sensor. Hyperion and future operational spaceborne hyperspectral data have better availability potential and may be used as a substitute for airborne hyperspectral data in some applications such as lithologic and mineral mapping. Compared with spaceborne multispectral instruments, hyperspectral sensors have several potential advantages. First, they can provide abundant spectral information and access to detailed spectral indexes based on surface reflectance, thus having better discrimination among similar materials. Second, they have an enhanced level of information for atmospheric correction to derive surface reflectance.

Spectral remote sensing has the potential to provide detailed information of mineralogy, chemistry and morphology of the Earth's surface as well as other celestial bodies such as Mars. The utility of hyperspectral and multispectral imagery for mapping surface geological compositions has been known for many years[6~11]. Lithologic, mineral assemblage and regolith mapping are some of the most prevalent applications of airborne hyperspectral data such as AVIRIS. A comparative study[12] between Hyperion and AVIRIS data for alteration rock mapping shows that the Hyperion imagery can also produce useful mineralogical information. Currently several digital image processing methods can be used for remote sensing geological information retrieval, including band ratios, log residuals, spectral curve matching, spectral classification and partial unmixing. A considerable body of literature has addressed the usefulness of airborne hyperspectral data in lithologic mapping and mineral discrimination of highly altered rocks[5,12,13], but with relative few studies using Hyperion to extract lithologic information for gold exploration in a low-angle-detachment-fault area.

The methods for lithologic/mineral mapping from hyperspectral imagery can be grouped as pixel and subpixel based. The former includes band ratios, log residuals, spectral angle mapper, spectral correlation mapper, spectral matching, and spectral classification. Subpixel analysis utilizes spectrally unique materials, termed endmembers[14] to unmix the mixed pixels in a scene to obtain subpixel compositions. These methods mainly include linear spectral unmixing[14,15], matched filtering[16,17], and mixture tuned matched filtering[18]. Most the state-of-the-art methods have been integrated in both RSI ENVI and ERDAS IMAGINE systems. The USGS TerraCoder is a typical implementation of spectral-shape matching.

The objective of the study is to examine the utility of Hyperion imagery in identifying gold-associated rock units in a low-angle detachment fault area[19]. An area of the southeastern Chocolate Mountains, California was used as a case study to demonstrate the utility of Hyperion data in identifying gold-related lithologic types. Pre-processing aspects of Hyperion data before it can be used for information retrieval is addressed first in Section 3. The dimensionality reduction of Hyperion cube and supervised classification were performed and are discussed in Section 4. Finally the research work is summarized and concluded in Section 5.

2 The Study Area and Geologic Setting

The southeastern Chocolate Mountains mineral district is located in the southeast part of Imperial County, California, centered about 16 miles north of Yuma in the extreme southeastern end of the Chocolate Mountains. The area contains the Picacho and Potholes districts and is bounded by the limits of the range on the south, by the Colorado River on the east and

north, and by the Carrizo Wash on the west[20]. From this district came the early mineral production of gold in California. The southeastern Chocolate Mountains district has been mined for lode and placer gold, silver, lead, and copper[19,20]. A subset of the Hyperion scene covers the middle part of this area from southwest to northeast. Fig. 1 shows the location of the study area and the generalized geologic map of the Hyperion coverage.

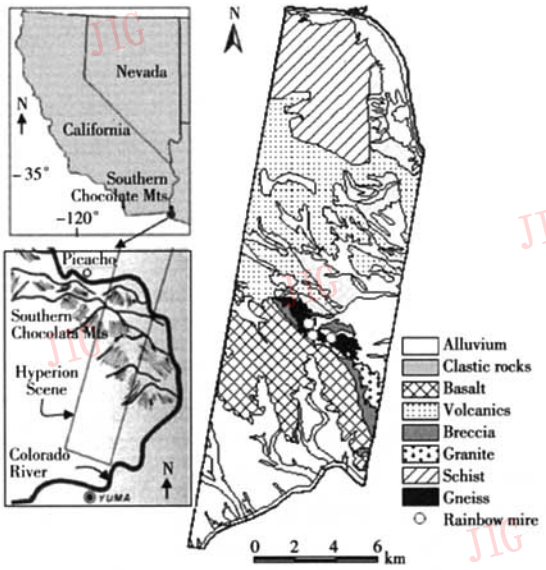

(a) The location of the study area　　(b) Generalized geologic map of the study area(after Morton 1977)

Fig. 1　The study area and geologic setting

The oldest rock unit exposed in this area is quartz biotite gneiss, which is tentatively correlated with the Precambrian Chuckwalla Complex (*mc*)[19,20]. The next youngest rock unit is Mesozoic Orocopia Schist (*mso*), which crops out in a several-square-mile area bordering the Colorado River from Picacho to Ferguson Lake. By far the most abundant rocks in the area are Tertiary volcanic rocks of widely variant composition and types. The Pliocene basalt flows (Tv^b) cap most of the mountains between Senator Wash and the southwestern limit of the range. Most of the volcanic and pyroclastic rocks (*Tv*) crop out in a wide west-northwest-trending belt extending from the Colorado River between Ferguson and Senator Wash all the way to the western limit of the southeastern Chocolate Mountains district. A small portion of unsorted early Tertiary sedimentary breccias (*Tbr*) and pre-Tertiary granitic rocks (*gr*) was observed at the southeastern corner of the study area.

The lode gold deposits of the district are pre-Tertiary in age; none of the volcanic rocks appear to be associated with the mineral deposits as they are in some other southern California areas[20]. Based on recent studies[19], the controls and origin of the deposits are largely related to "low-angle detachment faults". Most veins are deposited along distinct fault planes. Based on the analysis of the existing mines, prospecting for lode gold in the southeastern Chocolate Mountains district should be focused in pre-Tertiary metamorphic rocks, among which gneiss appears to be the more favorable host of gold deposits in the study area.

The gold mineralized gneiss is found immediately below the Tertiary volcanic rocks. Gneissic rocks (Chuckwalla Complex: *mc*) exposed in the study area are quartzofeldspathic gneisses which exhibit local variations in grain size, biotite content, and minor phase mineralogy[19]. To map these rock units (Tab. 1) is significant for searching for gold and understanding the regional geology. This study assessed the usefulness of EO-1 Hyperion satellite hyperspectral data for gold exploration by mapping related lithologic units in the district. For this purpose, one scene of Hyperion data acquired by the satellite EO-1 on April 9, 2002 was used.

Tab. 1　Significant lithologic units in the study area

Rock Types	Compositions	Training samples
Tc: Clastic rocks	moderately to poorly sorted, consolidated siltstone, sandstone, and conglomerate	412
Tv^b: Basalt flows	Fine-grained basalt and minor interbedded conglomerate	450
Tv/Tv^P: Volcanic rocks	Various volcanic rocks such as intrusive (Tv^i), pyroclastic (Tv^P), andesitic (Tv^a), etc.	460
Tbr: Tectonic breccia	Pale, gray-yellow, poorly sorted breccias, largely metavolcanic and metasedimentary rocks	410
gr: Granitic rocks	Biotite granite, leucigranite, quartz diorite, quartz monzonite	415
mso: Orocopia Schist	Sericite albite schist, quartz sericite schist, biotite schist, phillite, quartzite, and actinolite schist	475
mc: Chuckwalla Complex	Quartz diorite gneiss (*mc*), foliated hybrid granitic rocks, and granophyres	410

3 Preprocessing of Hyperion Data

The Hyperion VNIR sensor has 70 bands, and the SWIR has 172 bands, totaling 242 potential bands. Bands 1 to 7, 225 to 242, and the spectral band overlap region (bands 58 to 76) between the two spectrometers were intentionally not calibrated. As a result, only 198 bands have been provided in USGS Hyperion Level 1 products, and the other bands are set to zero values in the new USGS HDF format during the Level 1 processing[21]. Among the 198 bands, there are four remaining bands in the overlap between the two spectrometers. They are VNIR bands 56 (915.7nm) and 57(925.9nm), and SWIR bands 77 (912.5nm) and 78(922.6nm). Usually two of them are removed to obtain 196 unique bands. In this study, bands 8 to 56, and 78 to 224 were selected. Furthermore, by visual inspection of the 196 unique bands, the atmospheric water vapor absorption bands can be easily identified because almost all of the incident and reflected solar radiation were absorbed in these bands. The bands(121 to 126, and 167 to 178) were eliminated and the subset of 178 bands (quality level > 2 in Fig. 2) was obtained for further analysis in the study.

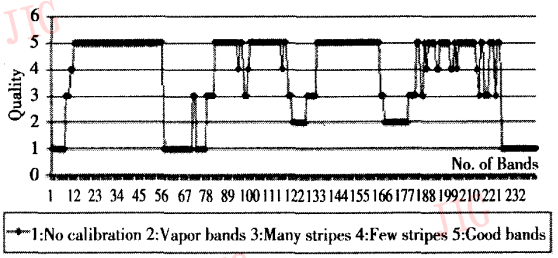

Fig. 2 Initial assessment of band quality of the Hyperion scene

The Level 1 product provided by USGS includes corrections that remove dark current bias effects and correction steps for "bad pixels". The pixel-and band-dependent calibrations have been adjusted over the life of the sensor and represent a well-balanced set of calibrations through effective use of solar, lunar, intersensor, and vicarious methods. However, there is some remaining noise such as vertical stripes and spectral "smile". Vertical stripes in particular need to be pre-processed prior to information extraction from the Hyperion image cube.

3.1 Destriping

For pushbroom instruments (e. g. Hyperion), a poorly calibrated detector in either the VNIR or SWIR arrays may leave a vertical "stripe" in a displayed image band[22]. This may be caused by factors such as detector nonlinearities, temperature effects, movement of the slit with respect to the focal plane, and calibration of some detectors with significantly modified gain and offset. Approximately 30% of the Hyperion image bands used in the study area has more or less vertical stripes. According to their appearance and digital numbers(DNs), the vertical stripes in Hyperion Level 1B products can be: continuous with a constant negative or positive DN, and intermittent patterns with different negative DNs or different positive DNs. The former are usually stronger and go through the whole columns, while the latter are relatively weak and discontinuous. As reported in literature, four methods are usually used to remove the vertical stripes of Hyperion Level 1 data: interpolation of the immediate left and right neighbors, histogram matching[22~24], forward-inverse minimum noise fraction (MNF) transformation, wavelet transformation[25], and Fourier transform[26]. The histogram matching method first constructs the histogram for each detector unit, and takes one response as the standard, the gain and offset for all other detector units are suitably adjusted and new DN values are computed[22,24]. The experiment shows that this approach can destripe the Hyperion image and produce good visual effect, but the change of original radiance values may distort the data and consequently reduces the classification accuracy. In the third method a forward MNF transformation is first used to "whiten" the striping noise and transform the noise into higher numbers of MNF bands. Low-frequency filters such as median filter may be then applied to the noise bands, or the noise bands are just set to zeros. A subsequent MNF inversion transformation is applied on the processed MNF bands, and the radiance data bands can be obtained with reduced stripes. This MNF transformation based approach is efficient for removing the aforementioned second type of image stripes, but some low probability information may also be taken as

noise and removed from the data set. Fourier transform can be used for noise removal but need much human interference during the processing of each band, thus it is very time-consuming.

The continuous stripes are usually very distinct and go through the entire columns. They are so strong that the MNF transformation even can't remove them. Thus, the average interpolation of the immediate left and right neighbors was used to replace the problematic columns in the study(Fig. 3).

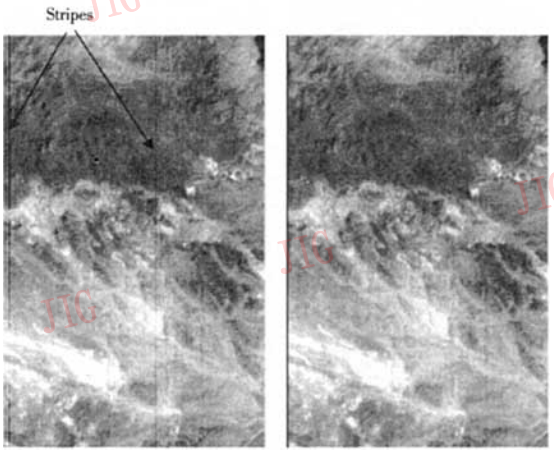

(a) before　　(b) after

Fig. 3　Removal of vertical stripes using interpolation

Bands 8 to 13, 94, 99, 116, 119, 137, 188, 193, 194, 200 to 203, 213, 214, and 222 were destriped using the interpolation approach. If the vertical stripes are caused by intermittent different positive or negative DNs, they were removed using the forward-inverse MNF transformation approach. A portion of the image of band 79 is used to show the effect of the destriping(Fig. 4).

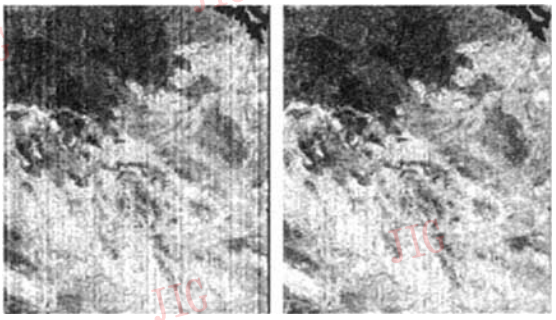

(a) before　　(b) after

Fig. 4　Removal of vertical stripes using MNF transformation

The destriping process significantly improves the visual effect of noisy bands. The MNF analysis shows that both the broad low-frequency effect and the local stripes have been reduced and the image is visually clean, and a higher number of MNF bands become clear as compared to the original MNF bands. Due to the fact that destriping processing may introduce new noise into the data set and subsequently reduce the accuracy of output from a classifier, some bands are very noisy such as 8, 9, 78 ~ 84, 97, 98, 119, 120, 127 ~ 133, 185, 186, and 224, and were also excluded from the data set. Consequently, only 154 bands were used for the further image analysis in the study.

3.2　Atmospheric Correction

Atmospheric correction is used to remove the atmospheric effects and transform the radiance at sensor to apparent surface reflectance. This correction is a prerequisite to most hyperspectral imagery data analysis approaches, especially when curve shape matching is made with laboratory or field spectra[12,27,28]. Three relevant atmospheric correction software packages are the Atmospheric REMoval program (ATREM), Atmospheric CORrection Now(ACORN), and the Fast Line-of-sight Atmospheric Analysis of Spectral Hypercubes(FLAASH). These programs are usually used to correct hyperspectral radiance data at sensor to surface reflectance in the analysis of hyperspectral data. Atmospheric correction methods basically follow the radiative transfer model[29], and each of the programs uses a slightly different version of algorithms. ACORN utilizes MODTRAN4 to estimate atmospheric parameters and calculate water vapor on a per-pixel basis[30]. ACORN is currently used for correction of both airborne and satellite hyperspectral data[31] and can produce high-quality surface reflectance without ground measurements[12]. The Hyperion data for the study area was converted to apparent reflectance using ACORN at the Remote Sensing Research Unit (RSRU), University of California at Santa Barbara. It appears that the atmospheric effects have been significantly reduced and the reflectance data can be used for further analysis(Fig. 5), though some artifacts have been introduced during the atmospheric correction.

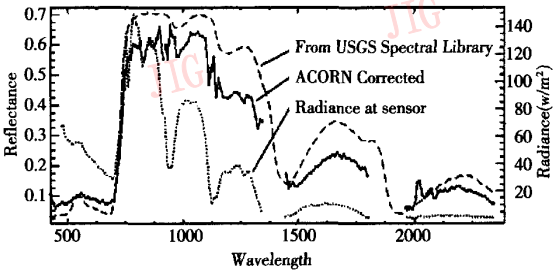

Fig. 5 Spectral curves of vegetation (green grass) from the Hyperion image before (at sensor) and after atmospheric correction using ACORN, and compared with a curve from the USGS spectral library

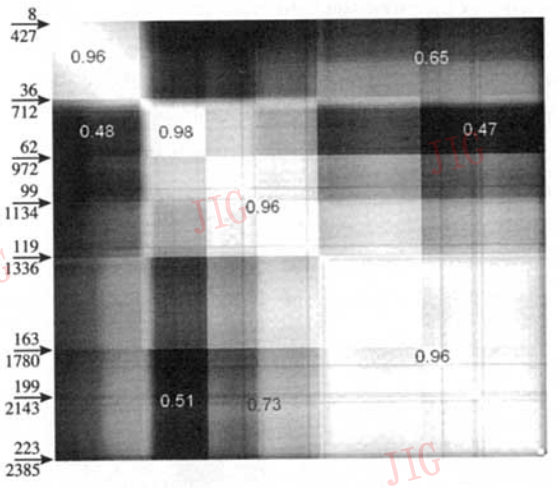

Fig. 6 Graphic representation of correlation matrix of the Hyperion data (The figures in the image indicate average correlation coefficients of the blocks, while the figures on the side denote band no. and the wavelength of the bands)

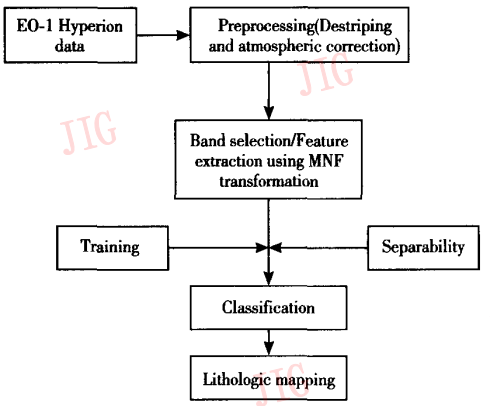

Fig. 7 Flowchart of Hyperion data classification using MLC

4 Extraction of Lithologic Units

4.1 Lithologic Classification

One drawback of maximum likelihood classifier (MLC) for hyperspectral imagery classification is the Hughes Phenomenon because of the limited training samples relative to the number of bands. For example, given 196 bands hyperspectral data, at least 197 pixels are mathematically necessary for calculating the covariance/variance. Another problem when applying MLC to data sets with high dimensionality is that it is difficult to make an accurate and stable estimate of the statistics for the data set[32]. Furthermore, hyperspectral data generally have larger data redundancy than multispectral data due to the narrow spectral sampling of the bands. Fig. 6 shows the data redundancy of the Hyperion data using correlation coefficient. The coefficients along the diagonal are close to one, which indicates higher information redundancy in the blocks, while the off-the-diagonal blocks have smaller average correlation coefficients, which indicates the bands in off-the-diagonal blocks are relatively more informative and less data redundancy. Thus, feature extraction prior to classification is significant for successful use of MLC. The approach for classifying the Hyperion imagery is illustrated in Fig. 7.

Minimum Noise Fraction (MNF) transformation[33] known as the noise adjusted principal components transformation, is used to reduce the dimensionality of the Hyperion cube and extract unique features for classification. The MNF transformation extracts information dimensions relative to an assumed noise structure in the hyperspectral data. After the transformation, the Hyperion data was "noise-whitened" and those MNF bands having eigenvalue of near one mainly contain noise[5,33]. Thus, the estimate of noise level is critical for MNF transformation. Here a "shift difference" method as implemented in the Environment for Visualizing Images (ENVI) system was utilized to estimate the noise level of the Hyperion cube. This method differences neighboring pixels directly above and to the right of the base pixel, then averages the values to obtain the base pixel's noise value[3]. This process derives an estimate of scene noise for use in the MNF transform.

The noise estimate gathered using the shift-difference statistics from a homogeneous area is better than that from the whole image[34]. A region of vegetation, water and homogeneous sand deposit was used as "homogeneous" areas to estimate the noise level of the Hyperion data, respectively. The three sets of resultant MNF bands have a different number of information bands and noise bands (Tab. 2). As shown in Tab. 2 more homogeneous samples can achieve a better estimate of noise level. An estimate of noise level derived from the vegetation sample or the whole image is relatively poor and provides less variance of the data. Based on the separability and visual check of the noise bands, as well as the similarity of the noise level between the samples and the image, 30 MNF bands using the sand samples to estimate the noise level can be extracted as features for the MLC classifier.

Tab. 2　Feature extraction based on different noise level estimates

Samples for Estimating the Noise Level	Water body	Green grass	Sand	Whole image
Sum of Eigenvalues	1 459	832	1 140	454
Number of MNF Bands at 90% Eigenvalue	56	72	46	104
Number of MNF Bands with >2.0 Eigenvalue	77	51	22	21

The training stage determines the performance of supervised classifiers to some extent because the statistics used in the MLC classifier is estimated from the training samples. Two factors are important in the training stage: the amount of training samples, and the variation of selected samples for a class[2,26,35]. The minimum number of training samples is a concern in supervised classification. A popular rule-of-thumb is that there should be at least 5D to 10D (D is the number of bands or features) training sample points for calculating the covariance/variance statistics[26,36]. Otherwise the singular covariance matrix problem may occur when the training sample size is not large enough relative to the number of bands used in the classification[32]. In the case of the Hyperion data classification, the MNF analysis was used to reduce the features involved in the classification. The second sensitive factor during the training stage is the representativeness of the training samples. Because of the large variation within a type of rock, the training sites should contain the sub-types of the same rock type. A stratification approach was adopted: first classifying the sub-types as different classes then merging them by post-processing. For example, the volcanic rock Tv can be slightly different because of the variation of mineral components, and subdivided into Tv^p, Tv^a, Tv^i, and Tv^{ia}. Because of the difficulty in collecting ground truth in some mountainous areas, and prohibited access to a military training ground in the study area, one-meter false color infrared aerial orthophotos were used to aid visual identification and orientation of surface features during the selection of the training sites in the study. To select a good set of training sites, the Bhattacharyya distance[37] is used to measure the separability during the training stage.

$$Bhat_{cd} = \frac{1}{8}(M_c - M_d)' \frac{V_c + V_d}{2}(M_c - M_d) + \frac{1}{2}\log_e \frac{\det \frac{V_c + V_d}{2}}{\sqrt{\det(V_c)}\sqrt{\det(V_d)}} \quad (1)$$

Where, M_c, M_d is the mean vector of class c, d respectively. V_c, V_d is the covariance matrix of classes c and d. The det operator is the determinant of a matrix.

In addition to the use of expert's knowledge and ground truth, the average Bhattacharyya distance was used to aid the selection of training samples. If a set of training samples can maximize the average Bhattacharyya distance among the classes in question, the training samples were used for the classification. It was also empirically found that about 400 sample points are optimal and a relatively stable estimate of the covariance/variance matrix can be produced in the case of 30 MNF bands involved in the classification process.

The training samples for the seven rock types in Tab. 1 were selected from the MNF bands of the Hyperion image. The 30 MNF bands were used as features and the MLC classifier was applied to extract the lithologic groups of the study area (Fig. 8 (a)).

Compared to the geologic map (Fig. 8 (b)), the significant lithologic units extracted from the Hyperion image data show excellent correlation with that in the reference map.

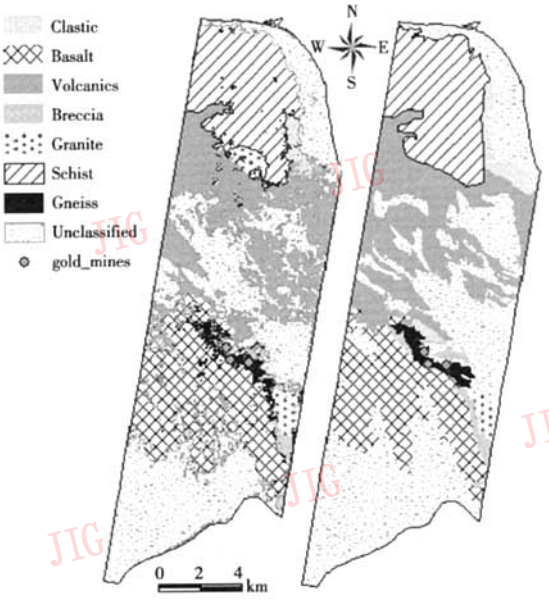

(a) Lithologic groups of the study area (b) Generalized geologic map (Morton 1977)

Fig. 8 Lithologic groups extracted from Hyperion data

4.2 Accuracy Assessment

In order to assess the classification accuracy, the classified image was geo-registered to the geographical reference system of the geologic map of the study area. An error matrix was generated for the MLC classification result (Tab. 3). The overall accuracy is 86.0% and a Kappa coefficient is about 0.81. The best identified lithologic groups are Orocopia Schist (*mso*), Granitic rocks (*gr*), Tertiary volcanic rocks (*Tv*), and Tertiary Basalt flows(Tv^b). The Producer's accuracy of these rock units are greater than 90%. But the User's accuracy of granitic rocks is very low. This is due to the fact that a rock unit in the northern part is identified as granitic rocks rather than mso because their spectral response is similar to rock type gr on the Hyperion image. It was proven by the field verification that the rock unit *gr* was not shown on the geologic map.

The Chuckwalla Complex(*mc*) is one of the main host rocks for gold deposits in the southeastern Chocolate Mountains area, but some *mc* areas were misclassified as rock Tv^b from the Hyperion scene. The mineral components of these two rocks are quite different and should be classified spectrally. Field investigation shows that the misclassification of these two rock types is caused by the following reasons: ① the narrow exposure of Chuckwalla Complex rock in the study area extends along the northwestern mountain slope, and is mostly overlain by the Tv^b rock debris. ② The weathering and varnish of the gneiss rock dilutes its spectral property. ③ Human disturbance (prospecting and mining) reworks and mixes the Tv^b, *mc*, Q_c and Tc^v rock types together. Consequently, the gneiss rock areas exhibit very similar spectral appearance to Tv^b on the Hyperion image, and they are difficult to distinguish from each other. The quaternary alluvium (Q_{al} and Q_c) are unclassified because they are insignificant for gold exploration.

Tab. 3 Accuracy of the MLC classification

	Rocks						
	Tbr	*gr*	*mc*	*Tc*	*Tv*	*mso*	Tv^b
User's	66	41	47	82	87	91	92
Producer's	35	95	64	36	91	90	91
Overall Accuracy = 85.96%				Kappa Coefficient = 0.81			

The case study in the southeastern Chocolate Mountains shows that certain lithologic groups can be extracted from the Hyperion data using the proposed approach. Also it highlights a problem with mapping *gr*: a unit of *gr* close to the rock *mso* is not mapped on the older geologic map.

5 Conclusion

This study investigated the utility of Hyperion imagery for lithologic mapping in a low-angle detachment fault area of the southeastern Chocolate Mountains, California. Maximum likelihood classification was used to extract lithologic units. The result shows that it is efficient for lithologic information extraction in the study area. The MLC classifier creates a "hard" classification with an overall accuracy of 86%. The study demonstrated that the MNF

transformation is useful to reduce the dimensionality of hyperspectral data, and the MNF bands with larger eigenvalues are usually extracted as classification features. In the study, the first thirty MNF bands were extracted for subsequent lithologic classification. In the case of 30 MNF bands used in the classification, approximately 400 sample pixels can produce a relatively stable estimate of the mean and covariance statistics. Using the average Bhattacharyya distance to measure the separability of the classes can aid the selection of "suitable" training samples in the analysis of the Hyperion data in the study area.

The vertical stripes which exist in Hyperion Level 1 data may occur as continuous entire-column negative or positive DNs, and as an intermittent columnar stripe pattern with different negative or positive DNs. The former is usually strong and occurs in relatively fixed column locations, while the latter exists in a more random way. If the entire-column stripes only exist in a few fixed columns, it is better to mask them out prior to further image analysis. However, in our case they were observed at 18 columns in the Hyperion image data of the study area. Thus they were removed by averaging the neighboring columns on the same band. With regards to the intermittent stripes in the Hyperion data, a forward-inverse MNF transformation was employed to reduce the stripe noise. The study shows that case-dependent destriping preprocessing can produce a better visual effect of the classification result and have little impact on the classification accuracy.

The successful utility of Hyperion data in lithologic mapping shows that Hyperion can achieve excellent lithologic discrimination in a low-angle-detachment-fault controlled geologic area. A comparative study performed by the authors in the same area shows that Hyperion data is more powerful in discriminating some small classes such as Tertiary breccia rocks than ETM and ASTER data. The resultant lithologic map can be used in gold exploration and regional geologic study in the south Chocolate Mountains area.

References

1 Vane G, Goetz A F H. Terrestrial imaging spectrometry: Current status, future trends[J]. Remote Sensing of Environment, 1993, **44**(2-3): 117 ~ 126.

2 Landgrebe D, Serpico S B, Crawford M M, *et al*. Introduction to the special issue on analysis of hyperspectral image data[J]. IEEE Transactions of Geosciences and Remote Sensing, 2001, **39**(7): 1343 ~ 1345.

3 Pearlman J, Carman S, Segal C, *et al*. Overview of the Hyperion imaging spectrometer for the NASA EO-1 mission[A]. In: Proceedings of IGARSS[C], Sydney, Australia, 2001, **17**: 3036 ~ 3038.

4 Ungar S G. Overview of EO-1, the first 120 days[A]. In: Proceedings of IGARSS, Sydney, Australian, 2001, **1**: 43 ~ 45.

5 Hubbard B E, Crowley J K, Zimbelman D R. Comparative alteration mineral mapping using visible to shortwave infrared (04-2.4μm) Hyperion, ALI, and ASTER Imagery[J]. IEEE Transactions of Geosciences and Remote Sensing, 2003, **41**(6): 1401 ~ 1410.

6 Crowley J K, Brickey D W, Rowan L C. Airborne imaging spectrometer data of the Ruby Mountains, Montana: mineral discrimination using relative absorption band-depth images[J]. Remote Sensing of Environment, 1989, **29**(2): 121 ~ 134.

7 Farrand W H, Harsanyi J C. Mapping the distribution of mine tailings in the coeur d'Alene River Valley, Idaho, through the use of a constrained energy minimization technique[J]. Remote Sensing of Environment, 1997, **59**(1): 64 ~ 76.

8 Farrand W H, Harsanyi J C. Mapping distributed geological and botanical targets through constrained energy minimization[A]. In: Proceedings of the Tenth Thematic Conference on Geological Remote Sensing[C], San Antonio, Texas, 1994: I-419 ~ I-429.

9 Sabins F F. Remote sensing for mineral exploration[J]. Ore Geology Review, 1999, **14**: 157 ~ 183.

10 Clark R N. Spectroscopy of rocks and minerals, and principles of spectroscopy[A]. In: King P L, Ramsey M S, Swayze G A (editors), Infrared Spectroscopy in Geochemistry, Exploration Geochemistry, and Remote Sensing[C], Mineralogical Association of Canada, London, 2005: 17 ~ 56.

11 Rowan L C, Mars J C. Lithologicmapping in the Mountain Pass, California area using advanced spaceborne emission and reflection radiometer(ASTER) Data[J]. Remote Sensing Environment, 2003, **84**(3): 350 ~ 366.

12 Kruse F A, Boardman J W, Huntington J F. Comparison of airborne hyperspectral data and EO-1 Hyperion for mineral mapping[J]. IEEE Transactions of Geosciences and Remote Sensing, 2003, **41**(6): 1388 ~ 1400.

13 Bierwirth P, Huston D, Blawett R. Hyperspectral mapping of mineral assemblages associated with gold mineralization in the central pilbara, western australia[J]. Economic Geology, 2002, **97**(4): 819 ~ 826.

14 Adams J B, Smith M O, Johnson P E. Spectral mixture modeling: a new analysis of rock and soil types at the Viking Lander 1 site[J].

Journal of Geophysical Research, 1986, **91**(B8): 8098 ~ 8112.

15 Keshava N, Mustard J F. Spectral unmixing[J]. Signal Processing Magazine, IEEE, 2002, **19**(1): 44 ~ 57.

16 Harsanyi J C, Chang C I. Hyperspectral image classification and dimensionality reduction: an orthogonal subspace projection approach [J]. IEEE Transactions on Geosciences and Remote Sensing, 1994, **32**(4): 779 ~ 785.

17 Boardman J W, Kruse F A, Green R O. Mapping target signatures via partial unmixing of AVIRIS data[A]. In: Green R O(ed) Summaries of the Fifth JPL Airborne Earth Science Workshop[C], JPL Publication 95-1, 1995, **1**: 23 ~ 26.

18 Boardman J W. Leveraging the high dimensionality of AVIRIS data for improved sub-pixel target unmixing and rejection of false positives: mixture tuned matched filtering[A]. In: Summaries of the Seventh Annual JPL Airborne Geoscience Workshop[C], Pasadena, CA, 1998.

19 Liebler G S. Geology and gold mineralization at the picacho mine, imperial county, california[A]. In: Bulk Mineable Precious Metal Deposits of the Western United States, Symposium Proceedings, the Geological Society of Nevada [C], Sockety of Nevada, Reno, Nevada, 1988: 453 ~ 472.

20 Morton P K. Geology and Mineral Resources of Imperial County[R]. County Report 7, California Division of Mines and Geology, 1977: 27 ~ 29.

21 Beck R. EO-1 User Guide (Version2. 3) [R]. Satellite Systems Branch, USGS Earth Resources Observation Systems Data Center (EDC), Sioux Falls, S. D., 2003: 74.

22 Datt B, McVicar T R, Van Niel, *et al*. Preprocessing EO-1 hyperion hyperspectral data to support the application of agricultural indexes [J]. IEEE Transactions on Geosciences and Remote Sensing, 2003, **41**(6): 1246 ~ 1259.

23 Horn B, Woodham R J. Destriping LandSat MSS images by histograms modification[J]. Computer Graphics Image Processing, 1979, **10**: 69.

24 Gupta R P. Remote Sensing Geology(2nd edition)[M]. New York, Berlin, Heidelberg: Springer-Verlag, 2003: 231.

25 Zheng L, Chan A K, Liu S, *et al*. Directional clutter removal of aerial digital images using X-ray wavelet transform and Markov random field[J]. IEEE Transactions on Geosciences and Remote Sensing, 1999, **37**(5): 2181 ~ 2191.

26 Jensen J R. Introductory Digital Image Processing: A Remote Sensing Perspective[M]. Prentice Hall Series in Geographic Information Science. Prentice Hall, Upper Saddle River, New Jersey, USA, 1996: 207.

27 Lewis M, Jooste V, de Gaspairs A A. Discrimination of arid vegetation with airborne multispectral scanner hyperspectral imagery [J]. IEEE Transactions on Geosciences and Remote Sensing, 2001, **39**(7): 1471 ~ 1479.

28 Nadeau C, Neville R A, Staenz K, *et al*. Atmospheric effects on the classification of surface minerals in an arid region using short-wave infrared hyperspectral imagery and a spectral unmixing technique[J]. Canadian Journal of Remote Sensing, 2002, **28**(6): 738 ~ 749.

29 Gao B, Goetz A F H. Column atmospheric water vapor and vegetation liquid water retrievals from airborne imaging spectrometer data[J]. Journal of Geophysical Research, 1990, **95**(D4): 3549 ~ 3564.

30 Kruse F A. Comparison of ATREM, ACORN, and FLAASH Atmospheric Corrections using Low-Altitude AVIRIS Data of Boulder, Colorado[A/CD]. In: Proceedings 13th JPL Airborne Geosciences Workshop[C], Pasadena, CA, 2004.

31 Analytical Imaging and Geophysics LLC (AIG). ACORN User's Guide, Stand Alone Version[R], Analytical Imaging and Geophysics LLC, 2002: 64.

32 Hoffbeck J P, Landgrebe D A. Covariance matrix estimation and *classification with limited training data*[J]. IEEE *Transactions on* Pattern Analysis and Machine Intelligence, 1996, **18**(7): 763 ~ 767.

33 Green A A, Berman M, Switzer P, *et al*. A transformation for ordering multispectral data in terms of image quality with implications for noise removal[J]. IEEE Transactions on Geosciences and Remote Sensing, 1988, **26**(1): 65 ~ 74.

34 RSI. ENVI User's Guide, The Environment for Visualizing Images [R]. Boulder, CO, 2003.

35 Lillesand T, Kiefer R. Remote Sensing and Image Interpretation [M]. New York, USA: John Wiley and Sons, Inc., 1999: 545.

36 Jain A K, Duin P W, Mao J. Statistical pattern recognition: a review [J]. IEEE Transactions on Pattern Analysis and Machine Intelligence, 2000, **22**(1): 4 ~ 37.

37 Fukunaga K. Introduction to Statistical Pattern Recognition[M]. New York, USA: Academic Press, 1990: 99.